Fluid Dynamics &
Materials Processing

Tech Science Press

http://doi.org/10.32604/fdmp.2026.078553

ARTICLE

Prediction of Liquid Film Development and Erosion-Corrosion Risk in Elbowed Pipeline Systems

Penghui Zhang[1,2], Nan Lin[2,*], Yang Wang[1,*], Ming Sun[2], Sixi Zha[1], Zongjie Zhou[1] and Chenglin Li[3]

[1]School of Mechanical Engineering, Xinjiang University, Urumqi, China
[2]Pressure Pipe Department, China Special Equipment Inspection and Research Institute, Beijing, China
[3]Karamay Bestar Technology Development Co., Ltd., Karamay, China
*Corresponding Authors: Nan Lin. Email: sy_linnan@163.com; Yang Wang. Email: wy830052@126.com

Received: 03 January 2026; Accepted: 12 May 2026; Published: 27 May 2026

ABSTRACT: Erosion-corrosion in refining and chemical plant pipelines remains a persistent integrity concern, particularly in straight sections located downstream of elbows, which are rarely prioritized in inspection programs that typically focus on elbows and tees despite their well-known vulnerability. In these downstream regions, developing flow structures can sustain wall impingement and liquid film formation, leading to progressive material loss that is often underestimated in practice. This work examines a representative industrial pipeline through a combined approach based on computational fluid dynamics (CFD) simulations and controlled experimental validation to resolve the hydrodynamic behavior in the straight pipe section downstream of an elbow under different operating conditions. The objective is to identify the governing parameters controlling liquid film development and to support predictive assessment of erosion-corrosion risk in overlooked pipeline regions. The analysis shows that liquid film length is primarily controlled by flow velocity, water volume fraction, and the length of the upstream vertical section. When the upstream vertical pipe length is below 1 m, the flow remains highly unstable after the elbow, promoting intensified wall interaction and increased erosion susceptibility. For larger upstream lengths, the liquid film length exhibits an approximately linear increase with water volume fraction. Its dependence on flow velocity is non-monotonic, increasing at lower velocities, reaching a maximum at 6 m/s, and decreasing thereafter. Building on these trends, a predictive correlation is developed for liquid film length as a function of water volume fraction, flow velocity, and pipe length. The resulting model provides a quantitative basis for identifying erosion-corrosion risk in straight pipe sections and supports more targeted inspection and integrity management strategies in industrial pipeline systems.

KEYWORDS: Numerical simulation; fluid dynamics; corrosion location prediction

1 Introduction

Owing to its economic advantages and excellent mechanical properties, carbon steel is widely used in oil and gas transportation pipelines; the presence of liquid phases can induce chemical reactions [1–3]. The flow of the medium inside carbon steel pipelines promotes the dissolution of the protective oxide film, leading to wall wear and thinning [4,5]. This process can be divided into two stages: first, soluble ferrous ions (Fe^{2+}) are generated at the oxide/water interface; subsequently, the corrosion products are transported through the diffusion boundary layer into the bulk fluid [6–8]. The corrosion location shifts with operating conditions. Generally, hydrodynamic parameters, pH, water temperature, and dissolved oxygen concentration are the primary factors influencing flow-accelerated corrosion [9–11]. Under actual

operating conditions, corrosion is governed by the synergistic effect of chemical and mechanical actions, making it difficult to accurately determine the specific causes and locations [12,13].

In recent years, research on flow accelerated corrosion (FAC) has advanced toward multi-field coupling, high-precision simulation, *in-situ* monitoring, and data-driven prediction, gradually becoming a research hotspot in corrosion protection and pipeline safety. Researchers have made progress in key areas, including the flow-mass transfer-electrochemical coupling mechanism, FAC interaction under complex media (CO_2/H_2S coexistence, sand-bearing erosion), coupled calculation of CFD and corrosion kinetic models, and machine learning-assisted corrosion rate prediction, which has significantly improved the prediction accuracy and prevention-control pertinence [14–18]. However, corrosion research on pipeline components still exhibits an obvious structural preference.

In practical production, elbows, tees, and straight pipes are the most common pipeline components. Among these, the flow field within elbows and tees undergoes significant variations with changes in flow direction and velocity [19], and the vigorous mass transfer process leads to a rapid increase in corrosion rate [20–22]. More research has focused on the corrosion behavior of elbows. Utanohara and Murase [23] experimentally studied the corrosion rate of elbow pipes under different flow rates and temperatures, and found that as flow rate increased, the FAC rate also rose in a nonlinear manner. Yoneda et al. [24] established correlation equations for geometric factors of elbows (curvature radius, bending Angle function) and the attenuation effect (spacing function) using CFD simulations, improving the prediction accuracy. Xiao et al. [25] built a relationship between temperature and flow-accelerated corrosion in carbon steel pipelines based on a steady-state FAC prediction model and compared their results with literature data. Zahedi et al. [26] proposed a simplified engineering model based on experiments and numerical simulations to rapidly estimate the mean liquid film thickness of annular flow at the 45° axial position (i.e., the mid-section) of a 90° elbow. Issa and Oliveira [27] developed a CFD-based predictive model capable of accurately simulating the liquid film distribution and gas-liquid separation process of annular flow in horizontal and vertical tee junctions. Xu et al. [28] analyzed the effects of various hydrodynamic parameters on FAC at elbows, and established an empirical model for predicting FAC in elbow pipes by integrating simulation and experimental results. Madasamy et al. [29] compared simulated flow rates with experimental wall thickness values obtained from ultrasonic measurements, demonstrating that the bend angle and bend radius play a critical role in FAC. Kim et al. [30] investigated FAC at welds and elbows, showing that combining an orifice with an elbow causes more severe corrosion than either feature alone.

Although the FAC mechanisms of special-shaped components such as elbows and tees have been relatively well studied, research on the corrosion behavior of medium flow in straight pipe sections remains insufficient and has not covered actual field conditions. In field operations, perforation cases have been reported in straight pipe sections downstream of elbows. Such failures are highly concealed and pose sudden risks, threatening to the safe production of oil and gas. To address these gaps regarding the flow corrosion mechanism and simulation validation in straight pipe sections, this paper carries out experimental research based on actual field conditions, calibrates and verifies the numerical simulation model, and systematically investigates the flow-accelerated corrosion behavior of straight pipe sections using FLUENT software. The results provide theoretical reference and technical support for preventing and controlling of flow-accelerated corrosion in carbon steel straight pipelines at oil and gas production sites.

2 Experiment

2.1 Experimental Conditions

An experimental platform was constructed based on the similarity principle, and a pipeline system experimental apparatus for multiphase flow accelerated corrosion studies was designed (as illustrated in Fig. 1). The system comprises three sections: a water supply section, a gas supply section, and an experimental section. For reasons of laboratory safety and cost considerations, air was substituted for natural gas in the gas supply section, and a stable gas source at a pressure of 0.8 MPa was provided by an air compressor. The gas was delivered to the test section via pipelines, with the flow rate measured by a flow meter and the gas intake regulated by adjusting the valve opening to achieve a uniform flow into the pipeline. Water was drawn by a diaphragm pump and introduced into the pipeline, with the liquid flow rate controlled through an adjustment knob. The detailed experimental parameters are presented in Table 1.

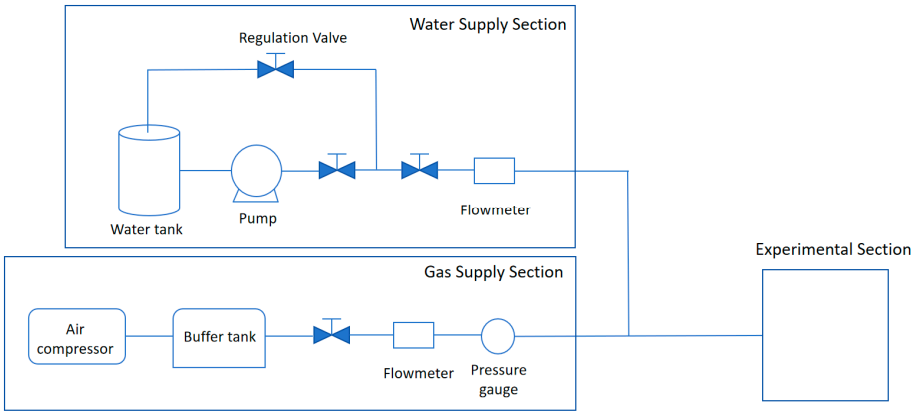

Figure 1: Experimental setup design.

Table 1: Experimental conditions.

Item	Initial Velocity (m/s)	Water Volume Fraction
value	4 5 6 7 8	0.07 0.14 0.21

Fig. 2 illustrates the experimental section: (a) shows the experimental apparatus, and (b) shows the geometric model. By classifying single-line diagrams of field installations, this paper summarizes the most frequent pipeline types and selects pipeline lengths based on the most common configurations observed in the installations. Owing to experimental limitations that prevent replication of full-scale field parameters, the pipe lengths and diameters were proportionally scaled down via geometric similarity. Key parameters of the experimental setup are summarized in Table 2. To facilitate flow visualization, transparent acrylic pipes were used for the critical flow observation sections, and a transparent graduated scale was affixed to the outer pipe wall for accurate dimensional measurement. The length of the upstream vertical pipe was set as the key variable in this study.

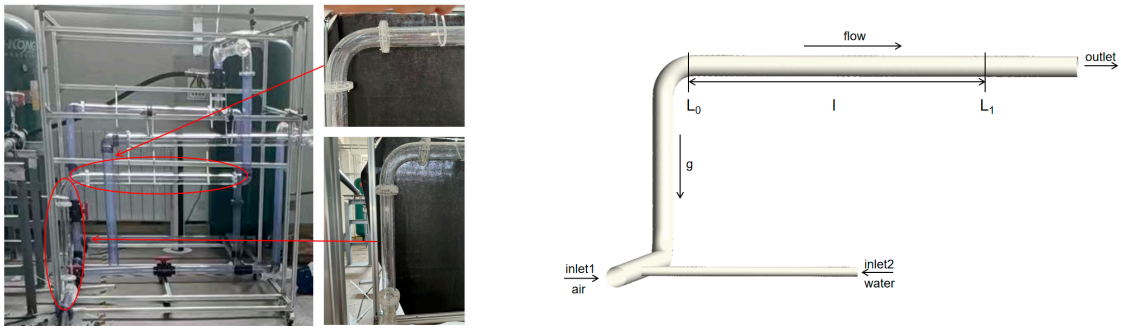

(a) Experimental pipeline **(b)** Geometric model

Figure 2: Experimental section setup.

Table 2: Setup parameters.

Item	Pressure (MPa)	Temperature (°C)	Pipe Diameter (mm)
Value	0.8	25	55

2.2 Experimental Results

2.2.1 Parameter Definition

Variations in liquid film length directly reflect the distribution characteristics of wall shear stress, mass transfer rate, and turbulence intensity in the straight pipe section. A longer liquid film adhesion length results in extended wall-fluid contact time, a more complete mass transfer process, and the continuous dissolution and spallation of the protective oxide film on the pipe wall by the flowing medium. Abnormal fluctuations in liquid film length correspond to abrupt changes in wall shear stress, which readily induce local turbulent scouring [31] and accelerate the corrosion process.

The length of the interface between the liquid film and discrete droplets on the upper pipe wall was selected as the key analytical index. As shown in Fig. 3. The direction of gravity is vertically downward. L_0 denotes the elbow-straight pipe junction, defined as the origin. L_1 denotes the liquid film-droplet interface, and l represents the liquid film length.

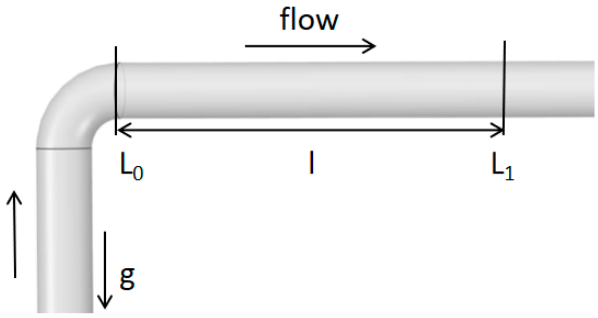

Figure 3: Schematic of liquid film length measurement.

In this study, liquid film length serves as a preliminary screening index for identifying corrosion-sensitive zones in the straight pipe section, enabling rapid identification of high corrosion risk zones in the straight pipe section downstream of the elbow, rather than a quantitative indicator directly characterizing the corrosion

rate. A key limitation is that it does not account for the effects of chemical parameters such as temperature and pH. Subsequent research will incorporate these parameters for a comprehensive analysis.

Prior to the experiments, a preliminary test was conducted to verify pipeline patency and airtightness, thereby ensuring stable operation of the apparatus. During the experiments, the flow fields at the elbow and the downstream horizontal straight pipe section were continuously observed, and the flow was considered to have reached a fully steady state when the flow morphology showed no discernible fluctuations for more than 5 consecutive seconds and the liquid film adhered stably to the downstream straight pipe wall. Once the flow reached the preset operating conditions and stabilized, images were captured with a high-speed camera for subsequent image analysis and measurement. The images were processed via frame-by-frame slicing, and liquid film formation was defined as the condition where the liquid film thickness on the upper wall of the downstream horizontal straight pipe reached 0.5 mm and was stably maintained. For each test condition, a total of 50 valid images were collected, and liquid film length data were extracted from each image; measurements with a deviation within 3 mm from the mean accounted for 80% to 85% of the total measurements, and the arithmetic mean of this valid data subset was taken as the final liquid film length reported herein. For the numerical simulation results, the water volume fraction on the upper wall of the downstream horizontal straight pipe was extracted for analysis; liquid film formation was defined as a local water volume fraction of 80%, with the liquid film length calculated accordingly.

2.2.2 Interpretation of Results

Fig. 4 shows the flow regime map of the gas-liquid two-phase flow in the vertical pipe from the experiments. In the upstream vertical pipe, the liquid phase undergoes an evolution from dispersion to accumulation and eventually to stabilization. An increase in inlet velocity, combined with sufficient upstream vertical pipe length, can accelerate this process; for pipe lengths shorter than 1 m, the degree of liquid phase dispersion is higher at a given flow velocity due to insufficient pipe length, which directly leads to anomalous variation in the liquid film length in this short pipe section. With increasing inlet velocity, the liquid phase accumulated faster, and the flow transitioned between stratified and annular flow regimes. The gas-phase drag force increases with rising inlet flow velocity. When the upstream vertical pipe length is sufficient ($\geq$1 m) and the flow velocity is less than 6 m/s, the breakup and dispersion effect of the gas-phase drag force on the liquid film in the vertical pipe intensifies, and turbulent vortices at the elbow entrain more of the liquid phase onto the upper wall of the downstream horizontal straight pipe section, causing the liquid film length to increase continuously with rising flow velocity. At an inlet flow velocity of 6 m/s, the gas-phase drag force reaches a dynamic equilibrium with gravity and surface tension acting on the liquid phase; under this condition, the turbulence intensity at the elbow is moderate, the attachment and spreading of the liquid phase on the upper wall of the downstream straight pipe section are most stable, the liquid film is uniformly distributed with no significant breakup, and consequently, the liquid film length reaches its maximum value. When the flow velocity exceeds 6 m/s, the gas-phase drag force substantially dominates over gravity and surface tension acting on the liquid phase. The excessively high turbulence intensity further breaks up the liquid film on the upper wall of the downstream straight pipe section into fine droplets, which are carried by the bulk gas flow, resulting in a reduction in the wall-attached length of the liquid film. Therefore, the liquid film length decreases with further increases in flow velocity above 6 m/s.

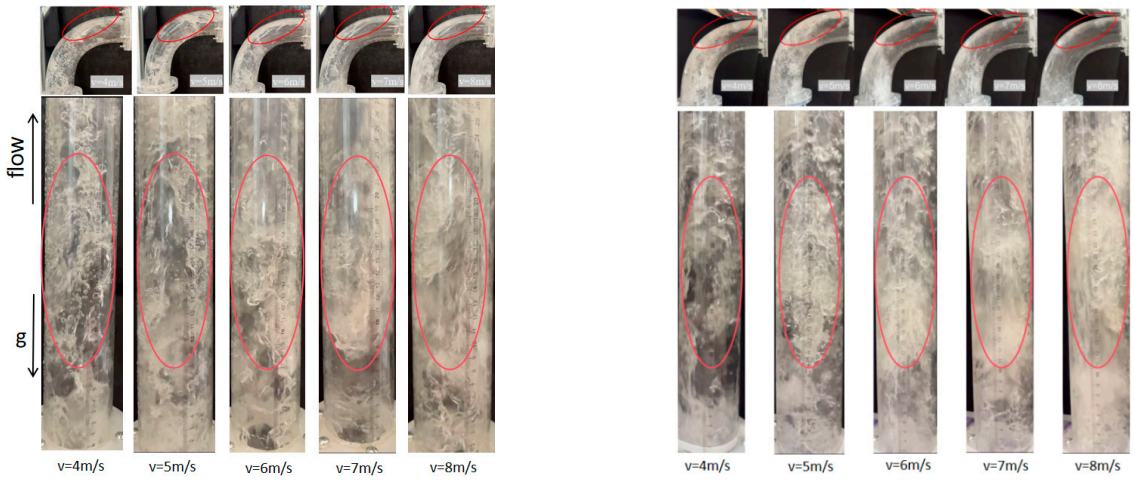

(**a**) Vertical pipe length: 0.5 m (**b**) Vertical pipe length: 1.5 m

Figure 4: Medium flow pattern.

Fig. 5 presents the variation curve of the liquid film length. The relationships among liquid film length, flow velocity, vertical pipe length, and water volume fraction are as follows:

(1) When the vertical pipe length and water volume fraction are kept constant, the liquid film length along the upper wall of the downstream horizontal straight pipe exhibits a trend of first increasing and then decreasing with increasing inlet flow velocity. As the inlet flow velocity increases to 6 m/s, the liquid film length reaches its peak value, and this velocity can be regarded as the critical inflection point for the evolution of the liquid film length.

(2) When the vertical pipe length was 0.5 m, the liquid film length along the upper wall of the downstream horizontal straight pipe showed no significant variation with increasing water volume fraction, indicating that the effect of water volume fraction on liquid film length is relatively weak under this condition. In contrast, when the upstream vertical pipe length exceeded 0.5 m, the liquid film length exhibited a distinct upward trend with increasing water volume fraction. As the water volume fraction increased to 0.14, the liquid film length reached a stable plateau, and further changes in water volume fraction no longer altered the liquid film length, suggesting that a water volume fraction of 0.14 corresponds to the saturation threshold for liquid film length growth.

When the vertical pipe length was 0.5 m and the flow velocity was less than 6 m/s, anomalous behavior was observed in the liquid film length. Further analysis indicates that this anomaly arises because the upstream vertical pipe length is insufficient to stabilize the flow, so that the liquid phase reaches the elbow while still in the liquid accumulation phase. In parallel, the local turbulence induced at the elbow by flow direction change exerts a more pronounced effect. The liquid phase tends to be entrained into the central pipeline flow region, rather than adhering to the elbow outer wall and flowing along the wall into the downstream horizontal straight pipe section. To clarify the underlying mechanism of these phenomena, the corresponding numerical simulation analysis is presented in the following sections.

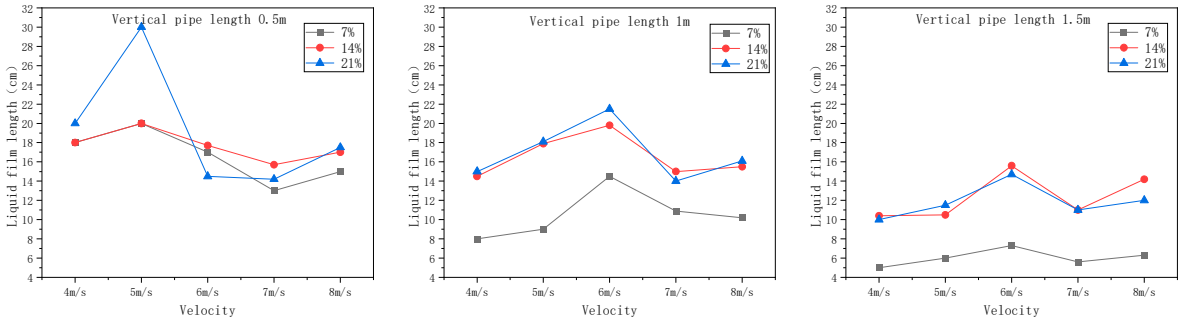

Figure 5: Variation in liquid film length.

3 Numerical Simulation

3.1 Geometric Model Establishment

To maintain flow conditions consistent with the experiments, the three-dimensional geometric model of the test section was constructed with identical dimensions to the experimental setup, as illustrated in Fig. 2b. The direction of gravity was vertically downward, with L_0 defined as the junction between the elbow and the straight pipe (zero reference point) and l representing the length of the liquid film adhering to the upper wall.

3.1.1 Governing Equations

Numerical simulations were performed using FLUENT to solve the three-dimensional transient incompressible Navier-Stokes equations. The gas-liquid two-phase flow was modeled using the Volume of Fluid (VOF) method to track the phase interface [32]. The core governing equations, including the phase volume fraction transport equation, mixture continuity equation, momentum equation, and closure relations for physical properties and surface tension, are detailed below:

(1) Phase Volume Fraction Transport Equation

In the VOF framework, the spatial distribution of the liquid and gas phases is characterized by the phase volume fraction α_q, which is defined as the ratio of the volume of phase q to the total volume of the computational cell. The volume fractions of the two phases satisfy the constraint:

$$\alpha_l + \alpha_g = 1 \tag{1}$$

In the equation: α_l: The liquid phase (water); α_g: The gas phase (air).

For each phase, the transport of the volume fraction is governed by the advection equation, which ensures the conservation of phase mass. For the primary liquid phase, the transport equation is written as:

$$\frac{\partial \alpha_l}{\partial t} + \nabla \cdot (\alpha_l u) = 0 \tag{2}$$

In the equation: u: The shared velocity vector of the gas-liquid mixture; t: Time; The gas phase volume fraction α_g is solved via the constraint in Eq. (1) to avoid numerical accumulation errors.

This transport equation is discretized using the Geo-Reconstruct scheme, which employs a piecewise-linear interface construction approach to maintain the sharpness of the gas-liquid interface and suppress numerical diffusion during advection.

(2) Mixture Physical Properties

The density ρ and dynamic viscosity μ of the gas-liquid mixture in each computational cell are calculated via volume-fraction weighted averaging, which is the standard closure for the VOF single-fluid model:

$$\rho = \alpha_l \rho_l + \alpha_g \rho_g \tag{3}$$

$$\mu = \alpha_l \mu_l + \alpha_g \mu_g \tag{4}$$

In the equation: ρ_l, μ_l: The density and dynamic viscosity of the liquid phase; ρ_g, μ_g: The density and dynamic viscosity of the gas phase.

For the effective Reynolds number calculation of the multiphase flow, the mixture properties at the inlet are adopted:

$$Re = \frac{\rho_{mix} v_{avg} D}{\mu_{mix}} \tag{5}$$

In the equation: Re: Effective Reynolds number of multiphase flow; ρ_{mix}: Equivalent density of the mixed fluid (kg/m^3); v_{avg}: The average flow velocity of the fluid in the pipe (4 m/s, Minimum set flow velocity at the inlet); D: Internal diameter of the pipeline (D = 0.055 m); μ_{mix}: The equivalent dynamic viscosity of the mixed fluid (Pa·s).

The minimum Reynolds number under the simulated conditions is calculated to be approximately 180,017, indicating fully turbulent flow in the pipeline.

(3) Continuity and Momentum Equations

The VOF method uses a single-fluid formulation, where a single set of continuity and momentum equations is solved for the gas-liquid mixture throughout the computational domain.

The mixture continuity equation is:

$$\frac{\partial \rho}{\partial t} + \nabla \cdot (\rho u) = 0 \tag{6}$$

The mixture momentum equation is:

$$\frac{\partial (\rho \mu)}{\partial t} + \nabla \cdot (\rho u u) = -\nabla p + \nabla \cdot \left[(\mu + \mu_t) \left(\nabla u + (\nabla u)^T \right) \right] + \rho g + F_\sigma \tag{7}$$

In the equation: u: The velocity vector, p: Pressure, g: Gravitational acceleration, F_σ: The surface tension force, μ_t: The turbulent viscosity.

(4) Surface Tension Force Formulation (Dependent on Interface Curvature)

The surface tension force is modeled using the Continuum Surface Force (CSF) mode, which converts the molecular surface tension acting on the phase interface into a volumetric body force in the cells containing the interface. This model is fully consistent with the VOF implementation in FLUENT, and its expression is directly dependent on the local interface curvature.

The volumetric surface tension force is written as:

$$F_\sigma = \sigma \kappa \rho \frac{\nabla \alpha_l}{\frac{1}{2}\left(\rho_l + \rho_g\right)} \tag{8}$$

In the equation: σ: The gas-liquid surface tension coefficient; κ: The local curvature of the gas-liquid interface, which is the core parameter governing the magnitude of the surface tension force.

The interface curvature κ is calculated from the divergence of the unit normal vector of the phase interface:

$$\kappa = -\nabla \cdot \hat{n} \tag{9}$$

In the equation: $\hat{n}$: the unit normal vector at the gas-liquid interface, defined as the normalized gradient of the liquid volume fraction:

$$\hat{n} = \frac{\nabla \alpha_l}{|\nabla \alpha_l|} \tag{10}$$

The curvature calculation is performed in the near-interface region ($0 < \alpha_l < 1$) to ensure that the surface tension force is only applied to the cells containing the phase interface, avoiding spurious numerical forces in single-phase regions.

(5) Turbulence Model Closure

To accurately capture the strong swirling flow, flow separation and boundary layer effects induced by the 90° elbow, the Realizable k-ε turbulence model was employed [33,34], which offers superior predictive performance for flows with strong streamline curvature and adverse pressure gradients compared to the standard k-ε model.

3.1.2 Numerical Solution Methodology

Pressure–velocity coupling was achieved using the PISO (Pressure-Implicit with Splitting of Operators) algorithm [35], which is well-suited for transient computations and effectively handles coupling issues with relatively large time steps. Regarding spatial discretization schemes: the gradient term was evaluated using the Least Squares Cell-Based method; the convective terms in the momentum and turbulence equations were discretized using a Second-Order Upwind scheme to ensure numerical accuracy; and the volume fraction equation was solved using the Geo-Reconstruct scheme to maintain a sharp gas-liquid interface. Temporal discretization employed a first-order implicit scheme, with a time step size set to 10^{-2} s. Within each time step, iterations were continued until the residuals fell below 10^{-5}.

Boundary conditions: The gas inlet was specified as a mass-flow inlet, while the liquid inlet was defined as a velocity inlet. The outlet was set as a pressure outlet (gauge pressure 0 Pa). All walls were assigned no-slip boundary conditions, and the contact angle was set to 60° (based on measured surface properties of the material). The k-ε turbulence equations were solved iteratively with a convergence criterion of 10^{-6}. The near-wall mesh was refined, with the first layer of near-wall grid cells having a height of 0.05 mm to ensure that the wall y^+ value remains within the range of 1–5, satisfying the requirements of the Enhanced Wall Treatment.

3.2 Grid Independence Analysis

The grid independence verification was conducted using the difference in fluid flow velocity along the horizontal direction of the straight pipe section downstream of the elbow as the criterion. The pipeline was discretized into several groups with varying grid numbers, and flow field simulations were performed. The flow velocity criterion was selected to generate the verification plot. The grid numbers were set to 316,373, 404,042, and 525,596, respectively, to verify grid independence. As shown in Fig. 6, it can be observed

that the difference between the grid number of 404,042 and that of 525,596 is relatively small, whereas the difference between the grid number of 316,373 and that of 404,042 is comparatively large. Accordingly, the grid with 404,042 cells was adopted for all simulations of the pipeline presented in this study. The mesh generation diagram is illustrated in Fig. 7.

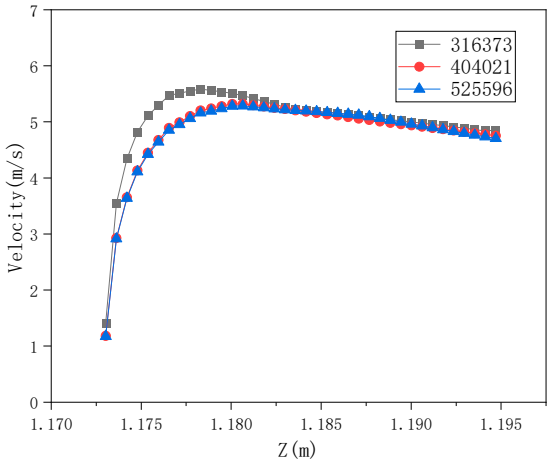

Figure 6: Grid independence test (using flow velocity difference as an indicator).

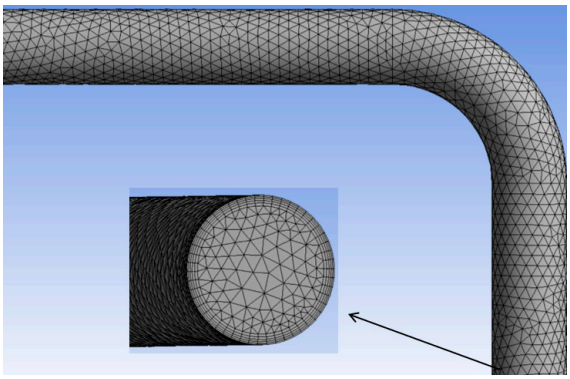

Figure 7: Grid division diagram.

3.3 Analysis of Results

3.3.1 Effect of Pipe Length

As illustrated in Fig. 8, with increasing upstream vertical pipe length, the fluid exhibits a distinct transition from an unstable to a stable flow regime. When the upstream vertical pipe length is 1 m, the fluid in the downstream half of the pipe reaches a fully stable state; however, when the upstream vertical pipe length reaches 1.5 m (the maximum value tested in this study), flow disturbances emerge in the region immediately upstream of the elbow. This flow behavior, arising from the combined action of variations in upstream vertical pipe length and local flow perturbations induced by the elbow, leads to the observed trend in which the liquid film length first increases and then decreases.

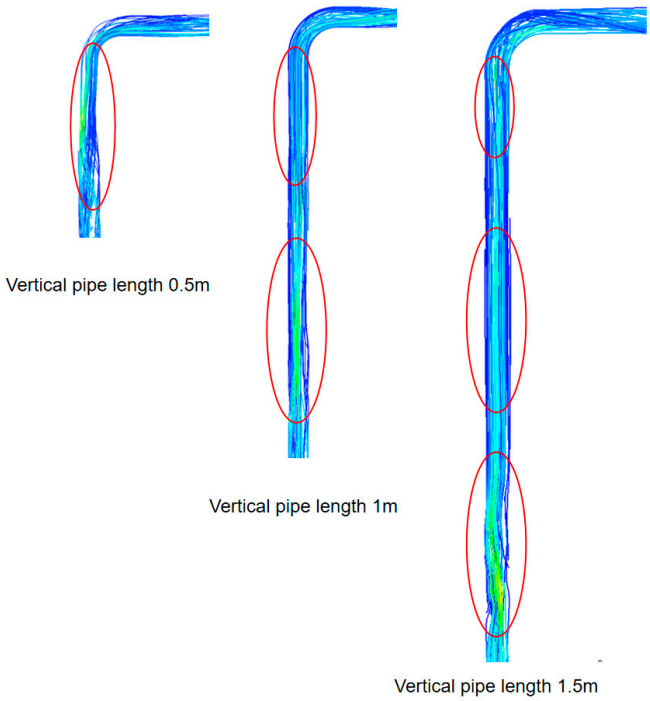

Figure 8: Trajectory diagram for different pipe lengths.

3.3.2 Effect of Water Volume Fraction

Figs. 9 and 10 display the phase distribution and velocity contour plots obtained for different water volume fractions. These contours clearly show that increasing the water volume fraction amplifies the effect of the elbow inner wall on the flow field, leading to a corresponding increase in the length of the liquid film adhering to the upper wall of the downstream straight pipe. This behavior arises because the liquid phase is acted upon by the combined effects of gravity and gas-phase drag, resulting in the formation of a non-uniform liquid film along the inner wall of the upstream vertical pipe. At low water volume fractions, no continuous, uniform thin liquid film can develop on the straight pipe wall; instead, the liquid phase predominantly exists as discrete droplets or localized liquid clusters, which settle and accumulate at the pipe bottom to form a thick water layer.

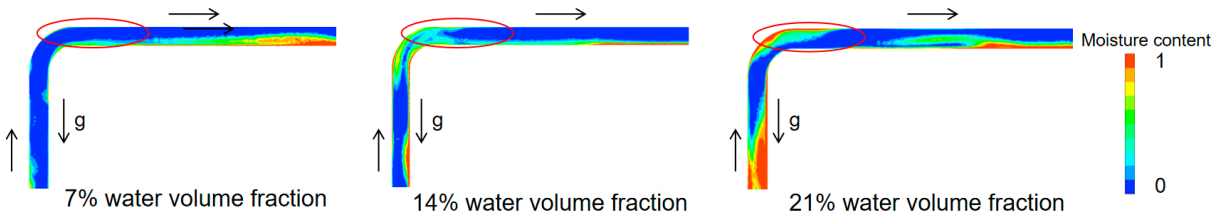

Figure 9: Phase-Mapped cloud diagram for a 1.5 m vertical pipe at 7 m/s velocity.

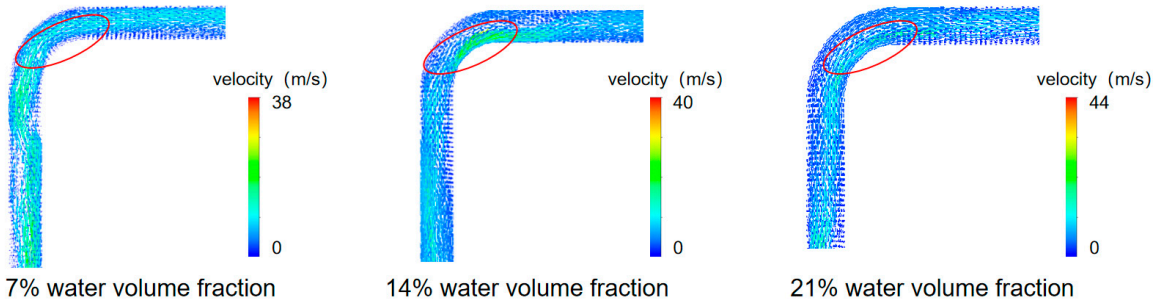

Figure 10: Velocity vector diagram for a 1.5 m vertical pipe.

3.3.3 Effect of Flow Velocity

When the pipe length exceeds 1 m, the fluid has already attained a stable state, and it can be observed from Fig. 11 that as the velocity increases, the length of the liquid film formed on the upper wall initially increases and subsequently decreases.

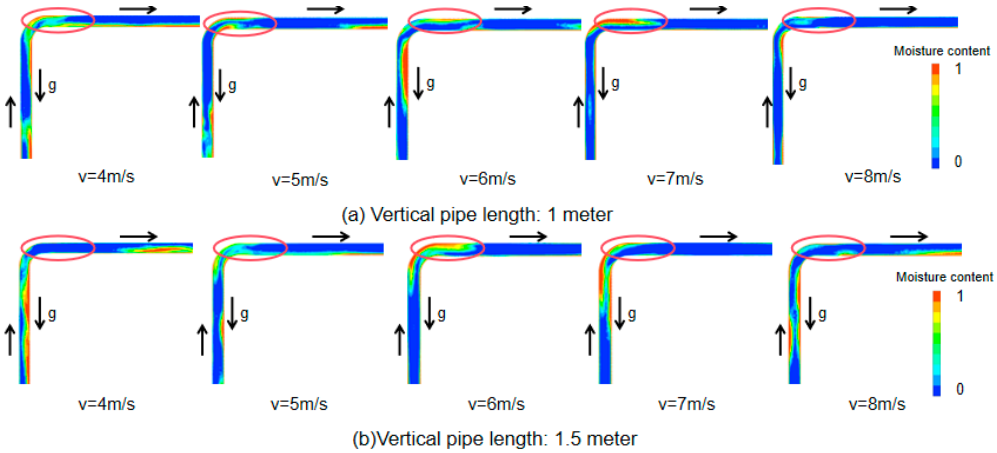

Figure 11: Phase distribution cloud diagram.

To quantitatively assess the predictive accuracy of the developed numerical model, we performed point-to-point extraction and statistical comparison between experimental and simulated data of liquid film evolution under various operating conditions. As shown in Fig. 12, the experimental (black) and simulated (red) curves are in excellent agreement across the full test range. Quantitative statistical analysis indicates that the simulated liquid film length has a mean relative error (MRE) of 2.9% against experimental measurements, a maximum absolute error (MAE) of less than 0.12 mm, and a maximum relative error limited to within ±4.5% for all operating conditions. Furthermore, deviations in key characteristic parameters (including liquid film peak position, fluctuation amplitude, and evolution rate) are all within 2%. These quantitative benchmarking results, evaluated from both numerical accuracy and feature matching perspectives, validate the reliability and precision of the established numerical model and its corresponding parameterization scheme.

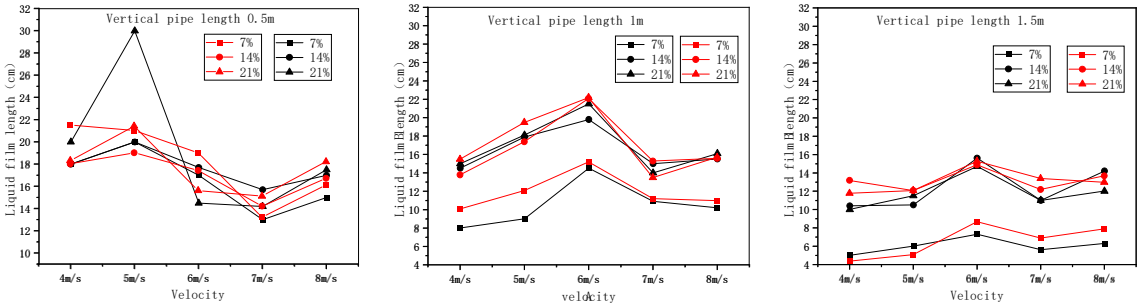

Figure 12: Comparison of liquid film change curves.

4 Model Development

Multiple sets of experimental and numerical simulation data were analyzed and fitted, confirming that water volume fraction, flow velocity, and vertical pipe length are all critical factors influencing the liquid film length on the upper wall of the pipeline. Significant differences were observed in the influence weights of each variable on the liquid film length. Undetermined coefficients were introduced to respectively adjust the influence weight and functional form of each variable, and a predictive model Formula (11) for liquid film length, encompassing the core variables of water volume fraction, flow velocity, and pipe length, was established.

$$L = \left(av^3 + bv^2 + cv + d\right)\frac{ek\omega}{l} \tag{11}$$

In the equation: L: Length of liquid film on upper wall (cm); v: Inlet velocity (m/s), with a range of $4 \leq v \leq 8$; ω: Water volume fraction (%), with a range of $7 \leq \omega \leq 21$; l: Length of vertical pipe (m), with a range of $0.5 \leq l \leq 1.5$; a, b, c, d, k, e are variable coefficients;

The coefficients presented in the formulas may vary for different pipeline models. For the model proposed in this study, the predictive formulas for liquid film length are given as (12) and (13), respectively. The fitting accuracy reaches 0.83, and further optimization may be achieved in subsequent work by incorporating the pipe diameter parameter.

$$L = \left(-0.05v^3 + 1.1v^2 - 6.0v + 12.5\right)\frac{0.825}{l}, l \leq 1, \left(k = \frac{1}{\omega}\right) \tag{12}$$

$$L = \left(-0.05v^3 + 1.1v^2 - 6.0v + 12.5\right)\frac{14.025\omega}{140l}, 1 < l \leq 1.5 \tag{13}$$

4.1 Sensitivity Analysis

The sensitivity coefficient S was adopted as a quantitative evaluation index to reflect the degree of relative change in the dependent variable induced by a unit relative change in the independent variable, and its formula is expressed as follows:

$$S = \frac{\Delta L/L_0}{\Delta x/x_0} \tag{14}$$

In the equation: S: The larger the sensitivity coefficient S of an independent variable, the more significant its influence on the liquid film length (i.e., the higher the sensitivity). $\Delta L/L_0$: The relative rate of change of the liquid film length $\Delta x/x_0$: The relative rate of change of the independent variable (L, v, ω);

A perturbation of ±10% was applied to each variable in the model (flow velocity, water volume fraction, and vertical pipe length) to analyze the corresponding rate of change in the liquid film length. The results indicate that flow velocity exhibits the highest sensitivity to liquid film length (rate of change: ±15%), followed by vertical pipe length (rate of change: ±12%), whereas water volume fraction shows the lowest sensitivity (rate of change: ±8%). These findings provide a reference for the adjustment of pipeline operating parameters in engineering practice.

4.2 Error Analysis

This study combines gas-liquid two-phase flow visualization experiments with CFD numerical simulations to investigate the liquid film distribution characteristics in the straight pipe section downstream of an elbow; inherent uncertainties and errors exist in both the experimental and simulation components.

Experimental errors are primarily divided into systematic and random components, with the core sources and corresponding mitigation strategies specified as follows:

(1) Errors in fluid parameter adjustment, arising from metering equipment inaccuracy and inlet pressure fluctuations, are minimized via pre-experiment calibration of all metering devices.
(2) Visualization measurement errors, originating from high-speed camera imaging deviations and image analysis uncertainty, are mitigated via dimensional scale calibration and strict outlier rejection during data processing.
(3) Inherent unsteadiness of the gas-liquid two-phase flow regime, an intrinsic source of random error, is suppressed by acquiring time-averaged flow morphology through continuous high-frequency imaging.

The overall numerical uncertainty in the simulations is primarily attributed to three sources, with corresponding mitigation strategies detailed below:

(1) Grid discretization error: An inherent numerical deviation, the magnitude of which is minimized via local mesh refinement in high-gradient critical regions and rigorous mesh independence verification.
(2) Model form error: Errors arising from empirical closure relations in the mathematical model, which are mitigated by calibrating model constants and correcting empirical coefficients against experimental data to ensure consistent trend agreement between simulated and measured results.
(3) Errors from boundary condition and phase interface simplification: Uncertainty introduced by the simplification of boundary conditions and VOF phase interface representation, the impact of which is suppressed by matching experimentally measured flow parameters and calibrating the phase interface discrimination criterion against high-speed experimental images.

Fig. 13 presents the error analysis plot for the liquid film length under various pipe lengths and water volume fraction conditions. From the figure, it can be observed that the errors do not alter the core variation trends of the liquid film length with respect to flow velocity, water volume fraction, and vertical pipe length, and are confined within an engineering acceptable range. Consequently, these errors do not compromise the scientific validity of the flow field mechanism analysis or the corrosion risk assessment. The findings of this study can provide a reliable basis for the prevention and control of flow-accelerated corrosion in carbon steel pipelines.

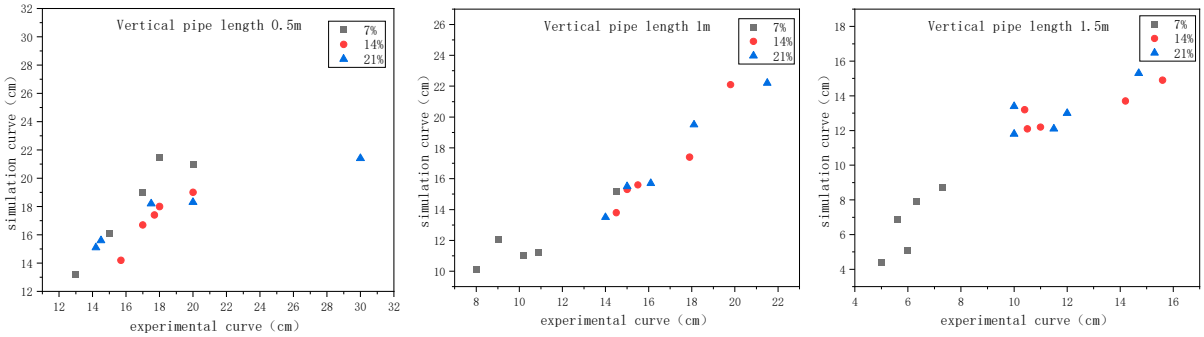

Figure 13: Error analysis diagram.

4.3 Analysis of Predictive Models

The predictive model was fitted and calibrated within the operating parameter range established in this study. The model delivers reliable predictions of the target liquid film length for engineering conditions consistent with those validated herein; however, its predictive accuracy may be compromised when parameters including pipe diameter, fluid properties, or flow conditions deviate from the validated calibration range. Future work will focus on further optimizing the model structure and empirical coefficients by expanding the simulated operating envelope and incorporating additional geometric and operating parameters (e.g., wider ranges of water volume fraction, upstream vertical pipe length, and pipe diameter). This will improve both the predictive accuracy and generalizability of the model for a broader suite of industrial pipeline applications.

Nevertheless, the model developed herein exhibits distinct advantages relative to the well-established classical EPRI FAC model. The EPRI framework uses parameters including fluid velocity, pipe material, and fluid chemistry to quantitatively predict the average corrosion rate of pipeline systems, with its core function centered on the "quantitative calculation of corrosion rate"; critically, however, it offers no inherent capability for spatial localization of high-risk corrosion-prone zones. In contrast, the predictive model developed herein uses liquid film length as its core diagnostic metric, is purpose-built for the precise spatial localization of corrosion-prone zones, and directly addresses and complements this well-documented limitation of the classical EPRI FAC framework.

5 Conclusions

This study is based on an actual industrial pipeline configuration, which was geometrically scaled down for both experimental tests and numerical simulations. The length of the liquid film-droplet interface on the upper pipe wall was adopted as a surrogate indicator for the actual corrosion risk of the pipeline. The experimental and numerical simulation data are in excellent agreement after direct comparison and data fitting, indicating that the proposed predictive model and corresponding parameter settings are reliable for guiding further research and engineering applications. Based on the above work, the following key conclusions are drawn:

(1) The variation of the liquid film length is correlated with the water volume fraction, flow velocity, pipe length. The influence of pipe length is particularly pronounced when the length is less than 1 m; under this condition, the fluid is in an unstable state and is more likely to cause wall impingement and erosion near the elbow. When the pipe length exceeds 1 m, the effect of the water volume fraction begins to manifest. As the water volume fraction increases, the liquid film length also increases gradually, exhibiting a linear relationship, and a threshold is reached when the water volume fraction attains 14%.

(2) Under the condition of sufficient vertical pipe length, the liquid film length initially increases and subsequently decreases with increasing flow velocity, and the liquid film length is relatively large when the flow velocity reaches 6 m/s. Analysis indicates that the fluid state within the pipeline is relatively stable under this condition.

(3) A predictive model was developed based on the experimental and numerical simulation data obtained in this study, incorporating key parameters including water volume fraction, flow velocity, and upstream vertical pipe length. The applicability of the proposed model is strictly limited to the validated operating conditions of this study, specifically a gas-liquid two-phase flow carbon steel pipeline with an inner diameter of 55 mm, a flow velocity range of 4–8 m/s, a water volume fraction range of 7%–21%, an upstream vertical pipe length range of 0.5–1.5 m, and a piping layout consisting of a 90° elbow directly connected to a downstream horizontal straight pipe section. Factors including variations in pipe diameter, fluid temperature, and water chemistry have not been incorporated into the current model. Applications beyond the above parameter space will require re-calibration of the model coefficients, and future work will incorporate parameters such as pipe diameter, temperature, and pH to further refine the model and extend its applicability.

(4) The corrosion assessment presented in this study is based on an indirect correlation between the liquid film length and corrosion-driving parameters and constitutes an exploratory analysis. The relevant conclusions are intended solely to provide a reference for corrosion risk control in engineering practice, rather than to establish a definitive corrosion law.

Acknowledgement: Sincere gratitude is extended to the supervisor for careful guidance throughout the research process. Thanks are also given to all teachers and peers for valuable suggestions and sincere help.

Funding Statement: This work was supported by the Sponsored by Key Special Project of the National Key R&D Program (2024YFC3810702), the Science and technology planning project of State Administration for Market Regulation (No. 2025MK131), Natural Science Foundation of Xinjiang Uygur Autonomous Region (No. 2022D01C389), the Xinjiang University Doctoral Start-up Foundation (No. 620321029).

Author Contributions: The authors confirm contribution to the paper as follows: study conception and design: Penghui Zhang, Nan Lin, Yang Wang, Data collection and organization: Penghui Zhang, Sixi Zha, Zongjie Zhou, analysis and interpretation of results: Penghui Zhang, Chenglin Li, Ming Sun, draft manuscript preparation: Penghui Zhang. All authors reviewed and approved the final version of the manuscript.

Availability of Data and Materials: The data used to support the findings of this study are available from the corresponding author upon request.

Ethics Approval: Not applicable.

Conflicts of Interest: The authors declare no conflicts of interest.

References

1. Heydari M, Javidi M. Corrosion inhibition and adsorption behaviour of an amido-imidazoline derivative on API 5L X52 steel in CO_2-saturated solution and synergistic effect of iodide ions. Corros Sci. 2012;61:148–55. [CrossRef].
2. Ahmed WH, Bello MM, El Nakla M, Al Sarkhi A, Badr HM. Experimental investigation of flow accelerated corrosion under two-phase flow conditions. Nucl Eng Des. 2014;267:34–43. [CrossRef].
3. Irshad HM, Toor IU, Badr HM, Samad MA. Evaluating the flow accelerated corrosion and erosion-corrosion behavior of a pipeline grade carbon steel (AISI 1030) for sustainable operations. Sustainability. 2022;14(8):4819. [CrossRef].

4. EPRI. Guidelines for controlling flow accelerated corrosion in fossil and combined cycle plants. Palo Alto, CA, USA: EPRI; 2005.
5. Kain V. Flow accelerated corrosion: Forms, mechanisms and case studies. Procedia Eng. 2014;86:576–88. [CrossRef].
6. Khunphakdee P, Chalermsinsuwan B. Review of flow accelerated corrosion mechanism, numerical analysis, and control measures. Chem Eng Res Des. 2023;197:519–35. [CrossRef].
7. Pietralik JM. The role of flow in flow-accelerated corrosion under nuclear power plant conditions. Jpn Soc Maintenology E J Adv Maint. 2012;4(2):63–78.
8. Tan Z, Yang L, Zhang D, Wang Z, Cheng F, Zhang M, et al. Development mechanism of internal local corrosion of X80 pipeline steel. J Mater Sci Technol. 2020;49:186–201. [CrossRef].
9. Bignold GJ, Garbett K, Garnsey R, Woolsey IS. 1. Erosion-corrosion in nuclear steam generators. In: Water chemistry of nuclear reactor systems 2. Leeds, UK: Thomas Telford Publishing; 1981. p. 5–18. [CrossRef].
10. Dooley RB, Chexal VK. Flow-accelerated corrosion of pressure vessels in fossil plants. Int J Press Vessels Pip. 2000;77(2–3):85–90. [CrossRef].
11. Kojo R, Kuroda Y, Kondo M, Tsuji Y. Flow accelerated corrosion and mass transfer rate in orifice downstream flow. In: Proceedings of the 14th International Topical Meeting on Nuclear Reactor Thermalhydraulics; 2011 Sep 25–30; Toronto, ON, Canada.
12. Islam MA, Jiang JJ, Xie Y, Fiala P. Investigation of erosion-corrosion behavior of (WTi)C based weld overlays. Wear. 2017;390–391:155–65. [CrossRef].
13. Senatore EV, Taleb W, Owen J, Hua Y, Gomes JACP, Barker R, et al. Evaluation of high shear inhibitor performance in CO_2-containing flow-induced corrosion and erosion-corrosion environments in the presence and absence of iron carbonate films. Wear. 2018;404–405:143–52. [CrossRef].
14. Wang Y, Lyu Z, Wu Z, Li L. Effect of fusion boundary microstructure on flow-accelerated corrosion cracking. Materials. 2024;17(9):2026. [CrossRef].
15. El-Gammal M, Mazhar H, Cotton JS, Shefski C, Pietralik J, Ching CY. The hydrodynamic effects of single-phase flow on flow accelerated corrosion in a 90-degree elbow. Nucl Eng Des. 2010;240(6):1589–98. [CrossRef].
16. Popova K, Prošek T. Mechanism of carbon steel corrosion in accelerated corrosion tests. Mater Corros. 2025;76(4):486–509. [CrossRef].
17. Wenpei ZH, Yingzheng LI, Yaru ZH, Taotao ZH, Xingtao LI, Shengyang YU, et al. An integrated corrosion rate prediction model based on global and local error fusion: A robust optimization strategy. J Chin Soc Corros Prot. 2024;45(2):523–32. (In Chinese).
18. Lee NY, Lee SG, Ryu KH, Hwang IS. On-line monitoring system development for single-phase flow accelerated corrosion. Nucl Eng Des. 2007;237(7):761–7. [CrossRef].
19. Moon S, Lee JY, Kim KM, Han SW, Lee GG, Maeng WY, et al. Hydrodynamic parameters affecting flow-accelerated corrosion in elbows. Nucl Eng Technol. 2025;57(4):103293. [CrossRef].
20. Efird KD. Disturbed flow and flow-accelerated corrosion in oil and gas production. J Energy Resour Technol. 1998;120(1):72–7. [CrossRef].
21. Madasamy P, Chandramohan P, Mukunthan M, Krishna Mohan TV, Rangarajan S, Uttam N, et al. Flow accelerated corrosion rate on carbon steel pipe bend by thin layer activation technique and computational modeling: Under PHWR operating conditions. Eng Fail Anal. 2021;121:105125. [CrossRef].
22. Hari Ponnamma R, Teegala D, Ravi Ranjan S, Kain V, Dipak Kumar B. Numerical simulation of turbulent flow in carbon steel pipes leading to flow accelerated corrosion. Arab J Sci Eng. 2014;39(8):6435–51. [CrossRef].
23. Utanohara Y, Murase M. Influence of flow velocity and temperature on flow accelerated corrosion rate at an elbow pipe. Nucl Eng Des. 2019;342:20–8. [CrossRef].
24. Yoneda K, Uchiyama Y, Morita R, Fujiwara K. Prediction of flow-accelerated corrosion in single/dual elbow in pipelines considering geometric parameters and layout effect. Mech Eng J. 2023;10(4):22–00344. [CrossRef].
25. Xiao Z, Wu J, Zhang T, Wang X, Chen W. Numerical simulation of temperature effects on flow-accelerated corrosion failure in carbon steel pipelines. Mater Prot. 2020;53(4):35–40. (In Chinese).
26. Zahedi P, Arabnejad Khanouki H, McLaury BS, Shirazi SA. Liquid film thickness prediction in elbows for annular flows. In: Proceedings of the Fluids Engineering Division Summer Meeting; 2017 Jul 30–Aug 3; Waikoloa, HI, USA. p. V01CT23A011. [CrossRef].

27. Issa RI, Oliveira PJ. Numerical prediction of phase separation in two-phase flow through T-junctions. Comput Fluids. 1994;23(2):347–72. [CrossRef].
28. Xu T, Zhang R, Si X. Effects of fluid dynamics parameters on flow-accelerated corrosion at elbow of carbon steel pipeline. Mater Res Express. 2024;11(5):056520. [CrossRef].
29. Madasamy P, Mukunthan M, Chandramohan P, Krishna Mohan TV, Sylvanus A, Natarajan E, et al. Influence of bend geometry on flow accelerated corrosion under neutral pH conditions. Eng Fail Anal. 2021;122:105127. [CrossRef].
30. Kim DJ, Kim SW, Lee JY, Kim KM, Oh SB, Lee GG, et al. Flow-accelerated corrosion assessment for SA106 and SA335 pipes with elbows and welds. Nucl Eng Technol. 2021;53(9):3003–11. [CrossRef].
31. He S, Ariyaratne C, Vardy AE. Wall shear stress in accelerating turbulent pipe flow. J Fluid Mech. 2011;685:440–60. [CrossRef].
32. Hirt CW, Nichols BD. Volume of fluid (VOF) method for the dynamics of free boundaries. J Comput Phys. 1981;39(1):201–25. [CrossRef].
33. Van Doormaal JP, Raithby GD. Enhancements of the simple method for predicting incompressible fluid flows. Numer Heat Transf. 1984;7(2):147–63. [CrossRef].
34. Shih TH, Liou WW, Shabbir A, Yang Z, Zhu J. A new k-ϵ eddy viscosity model for high reynolds number turbulent flows. Comput Fluids. 1995;24(3):227–38. [CrossRef].
35. Issa RI. Solution of the implicitly discretised fluid flow equations by operator-splitting. J Comput Phys. 1986;62(1):40–65. [CrossRef].